ICG-Loaded PEG-Modified Black Phosphorus Nanosheets for Fluorescence Imaging-Guided Breast Cancer Therapy

Wanwan Pan,[#] Weijian Chen,[#] Yuanzeng Min, Jing Wang, Zhenye Yang,* Tian Xu, Fazhi Yu, Guodong Shen,* Yuan Hu,* and Xiaopeng Ma*

Read Online

ACCESS | Metrics & More | Article Recommendations | Supporting Information

ABSTRACT: Indocyanine green (ICG) has been used in various surgical navigation systems and plays an important role in intraoperative imaging diagnosis. However, the poor photostability and unsatisfactory tumor-targeting ability have limited its broad application prospects. In the decades, the construction of a nanodrug delivery system for tumor-targeting diagnosis and therapy has become a research hotspot. Black phosphorus nanosheets (BPNS), as a new kind of biodegradable nanomaterials, have the advantages of high loading capacity, good biocompatibility, tumor targeting, and photothermal effect over other two-dimensional (2D) reported nanomaterials. Herein, ICG-loaded poly(ethylene glycol) (PEG)-modified BPNS (ICG@BPNS-PEG) nanocomposites are constructed to improve the tumor-targeting capacity and guide photothermal therapy through real-time fluorescence imaging. In this study, ICG@BPNS-PEG nanocomposites with a suitable size (240 ± 28 nm) have been successfully constructed. The photostability of ICG@BPNS-PEG nanocomposites surpassed that of free ICG after four on−off cycles of near laser irradiation (NIR). Moreover, ICG@BPNS-PEG nanocomposites have enhanced photothermal conversion ability. The cellular uptake result through flow cytometry showed that ICG@BPNS-PEG nanocomposites could be swallowed easily owing to the suitable size and passive cellular uptake. In addition, the cytotoxicity evaluation of MCF-7, 4T1 breast cancer cells, and healthy RPE cells through the MTT assay demonstrated that ICG@BPNS-PEG nanocomposites have lower cytotoxicity and good cellular compatibility without irradiation. However, the cytotoxicity and live/dead staining proved that ICG@BPNS-PEG nanocomposites have satisfactory photothermal therapeutic effects when irradiated. In the 4T1-bearing mice model, the fluorescence imaging after intravenous injection of nanocomposites showed that ICG@BPNS-PEG nanocomposites have superior passive tumor targeting accumulation through the enhanced permeability and retention (EPR) effect compared with that of free ICG. Also, changes in tumor volume showed a remarkable tumor growth inhibition effect compared with other groups. Moreover, the results of hematoxylin−eosin (H&E) staining of major organs in 4T1-bearing mice also demonstrated that the nanocomposites have good biocompatibility. Therefore, the constructed ICG@BPNS-PEG nanocomposites have substantial potential in breast cancer therapy.
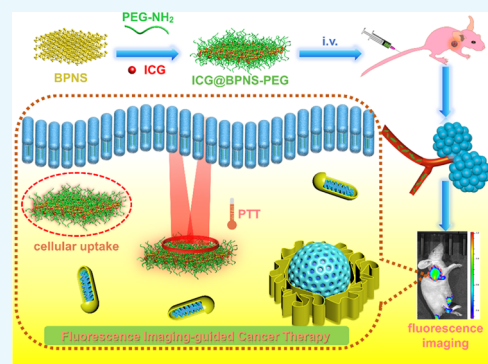
INTRODUCTION

Breast cancer is the most common malignant tumor in women worldwide and is one of the leading causes of women's death in cancers.[1] Nowadays, the main clinical therapy methods include surgery, radiotherapy, and chemotherapy.[2] However, incomplete resection of the surgical site, poor tumor-targeting chemotherapeutics, and side effects of neoadjuvant chemotherapy (NAC) affect the efficacy of breast cancer treatment.[3] Integrating diagnosis and therapy is a new treatment mode. Fluorescence imaging diagnosis to guide treatment increases the accurate therapeutic effect of tumors. Due to the biodiversity of the material, the widespread application of this treatment mode is optional.

Indocyanine green (ICG) is a near-infrared (NIR) fluorescent dye approved by the U.S. Food and Drug Administration for clinical application.[4] It could be excited by external light with a wavelength of 750−810 nm after ICG was injected into the human body and emitted NIR light of the wavelength of ~850 nm. At present, ICG has been used in a variety of fields such as fluorescence imaging diagnosis.[5] It has mature clinical applications in liver tumor removal, retinal angiography, cardiovascular function, and breast cancer sentinel lymph node exploration.[6,7] In addition, it can efficiently absorb NIR light and convert it into thermal energy for photothermal therapy (PTT).[8] However, ICG is unstable and decomposes rapidly upon exposure to air. Also, it is more easily decomposed in the light environment and has a high metabolism, low cell
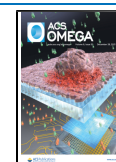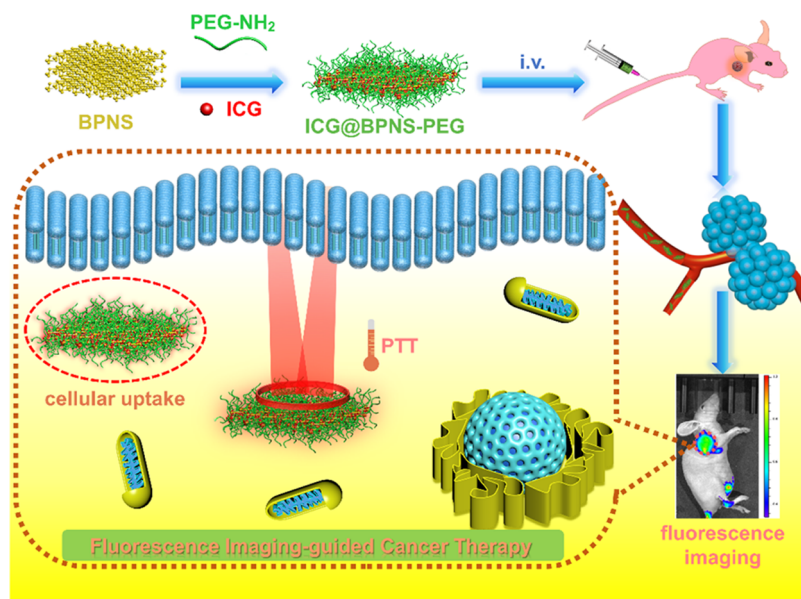
Figure 1. Illustration of preparation and fluorescence imaging of tumor locations of ICG@BPNS-PEG and fluorescence imaging-guided cancer photothermal therapy.
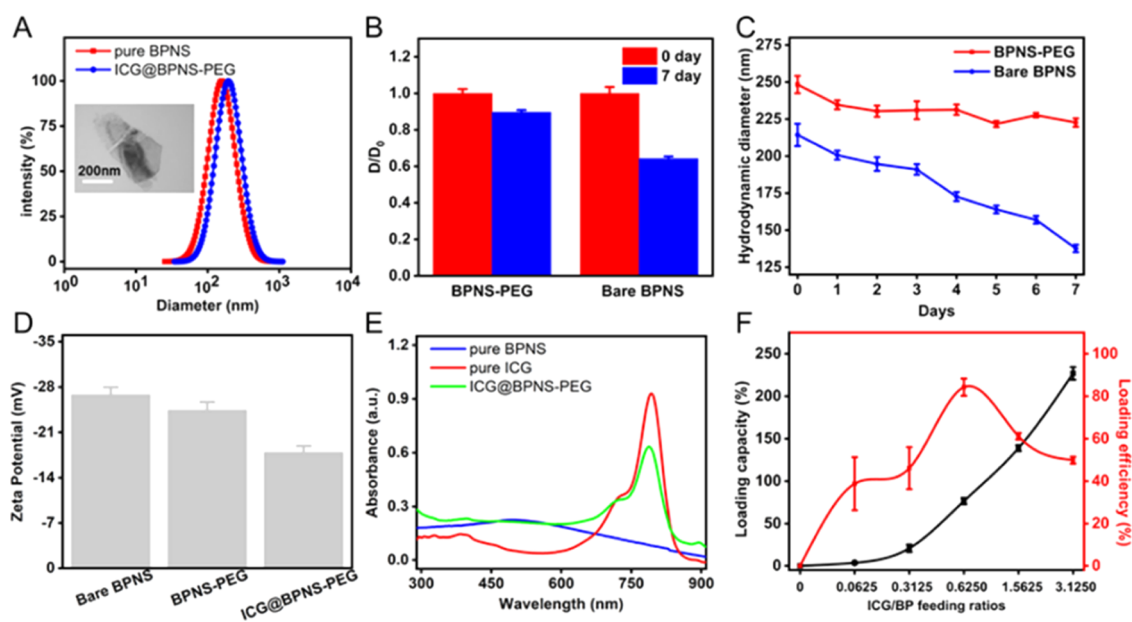
Figure 2. (A) DLS and TEM image of ICG@BPNS-PEG. (B) The corresponding diameter on 0 day to that on 7 days. (C) The corresponding change in the hydrodynamic radius of various samples bearing air at room temperature in 1 week. (D) ζ-Potential of various samples. (E) UV−vis absorption of various samples. (F) Loading capacity and loading efficiency with the ICG/BP feeding ratio.

absorption rate, and so on.[9,10] Therefore, these characteristics limit the effective application of ICG in biological diagnosis and treatment.

In recent years, nanomaterials have been widely used in biomedical fields.[11−14] This idea finds its most significant application in PTT, where functionalized nanomaterials have been used to demonstrate selective tumor targeting accumulation and drug delivery.[15,16] Black phosphorus (BP), a new kind of two-dimensional nanomaterial, has become a research hotspot. With the wide application of nanomaterials in the field of biomedicine, BP, as a drug carrier in tumor diagnosis and treatment has received extensive attention owing to the enhanced permeability and retention (EPR) effects. It has excellent properties in electronics, optics, and so on. Compared

with other two-dimensional nanocarriers, black phosphorus nanosheet (BPNS) has the advantages of an adjustable visible-light absorption band, excellent photothermal conversion efficiency, and nontoxic side effects of degradation products on the body.[17] They have been widely used in tumor diagnosis and treatment because of their highly effective drug loading capacity. Compared with small molecular carriers such as liposomes and polymer carriers, BPNS carriers have significant advantages of biological safety, good drug loading, easy surface modification, and so on. Owing to the limitations of surgical therapy, chemotherapy, radiotherapy, or other methods in tumor therapy, PTT has attracted increasing attention from many researchers.[18] PTT has emerged as a new tumor therapy method. Under the irradiation of NIR light, the tumor location
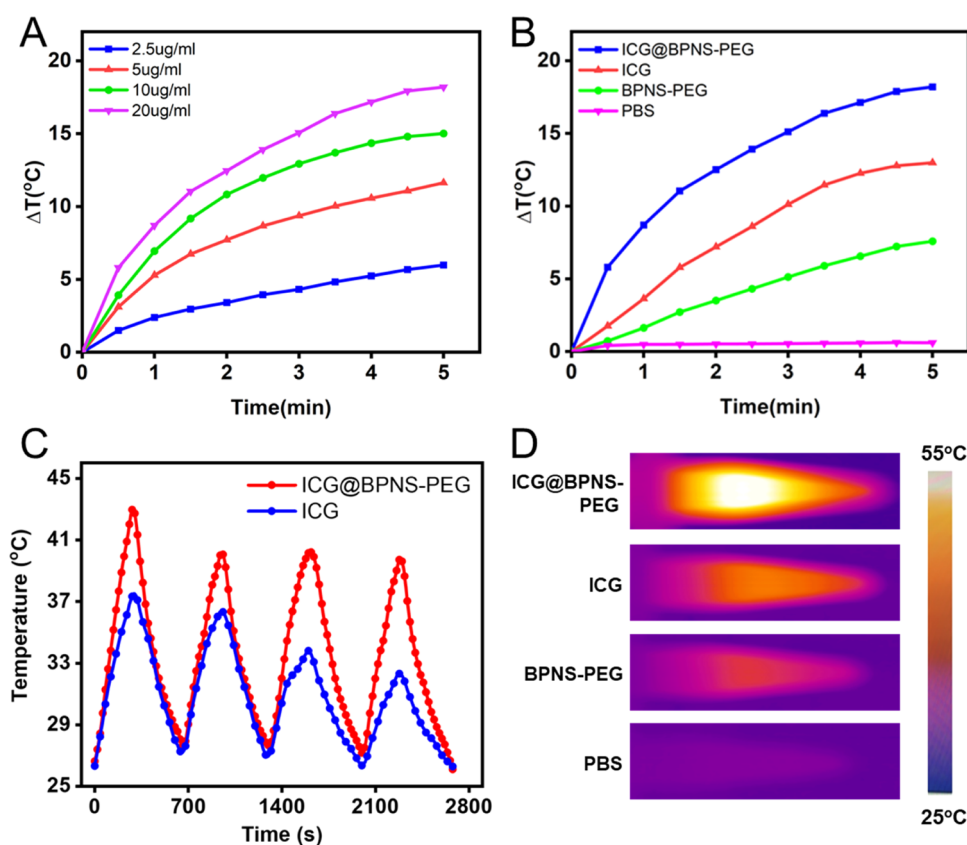
Figure 3. In vitro photothermal performances of PBS, ICG, BPNS, and ICG@BPNS-PEG. (A) Temperature variation curves of the ICG@BPNS-PEG solution under different concentrations after treatment with 808 nm NIR laser (1.65 W/cm^2, 5 min). (B) Photothermal heating curves of PBS, ICG, BPNS, and ICG@BPNS-PEG (1.65 W/cm^2, 5 min). (C) Heating curve of suspension of the ICG@BPNS-PEG and ICG solution for four on−off cycles with an 808 nm NIR laser (1.65 W/cm^2, 5 min). (D) NIR thermal images of PBS, BPNS, ICG, and ICG@BPNS-PEG solution with continuous 808 nm NIR laser irradiation (1.65 W/cm^2, 5 min).

converts absorbed light energy into heat energy, using high temperatures to kill cancer cells.[19,20] Currently, various nanomaterials have been used for PTT,[21,22] including graphene, BP Mxenes.[23−26] At the same time, accurate diagnosis and therapy of breast cancer is currently an important developmental direction in clinical research.[27] Therefore, the construction of a nanodrug delivery/fluorescence system to achieve the integration of tumor-targeting imaging diagnosis and treatment has become a research boom.

Herein, we constructed an ICG@BPNS-PEG nanosystem that integrates real-time fluorescence imaging of tumor location with PTT principles for breast cancer therapy. As shown in Figure 1, fluorescence imaging agent ICG is integrated into black phosphorus nanosheets via physical interaction and modification of PEG enhances the stability in PBS and blood as well as protects BP and ICG from oxidation. After intravenous injection, the constructed nanosystem is accumulated and uptaken, followed by fluorescence imaging-guided cancer photothermal therapy. Our study results also show that constructed ICG@BPNS-PEG has the advantages of stability, tumor-targeting accumulation, and PTT of ICG.

RESULTS AND DISCUSSION

The preparation method of BPNS was modified according to the top-down method. By controlling the ultrasonic parameters, the proper BPNS with ~200 ± 15 nm were harvested and also showed a narrow size distribution that the polydispersity coefficient of 0.245 as shown in Figures 2A and S1A. Meanwhile,

the Raman spectroscopy and X-ray powder diffraction (XRD) patterns of bulk BP and BPNS are presented in Figure S1B,C. As shown in Figure S1B, for bulk BP, three Raman vibration modes located at 360.4, 439.5, and 466.1 cm^{-1} were attributed to the A_{1g}, B_{2g}, and A_g^2 modes, respectively. Also, BPNS showed a slight red-shift (around 2−3 cm^{-1}) compared with the bulk BP, indicating that the bulk material has been successfully exfoliated into few-layer BPNSs. Meanwhile, the (0 2 0), (0 2 1), (0 4 0), and (0 6 0) lattice planes of BP appeared in Figure S1C, which indicates that the host structure of BP crystal is not altered. Especially, the appearance of the characteristic diffraction peak at 35.4° corresponding to the (1 1 1) crystal plane confirms that bulk BP is successfully exfoliated into few-layered nanosheets. The above satisfactory results indicate that the few-layered BPNS is successfully exfoliated.

Inspired by the electron-rich characteristics on the surface of BPNS, the fluorescent diagnostic molecules indocyanine green (ICG) in the clinical setting were anchored on the surface of BPNS through hydrogen bonding and $\pi-\pi$ conjugation. However, some researchers found that the BPNS directly peeled from the BP crystals are easily phagocytosed by the liver and have difficulty reaching the tumor location, and they can be quickly degraded.[28,29] Therefore, the hydrophilic segments PEG-NH$_2$ were integrated into the nanocomposites to improve the stability of the binding components of BPNS and ICG in an aqueous solution. The larger hydrodynamic radiuses reach up to 240 ± 28 nm in Figure 2A, which is consistent with that of the TEM image. Moreover, PEG coating also plays an essential role
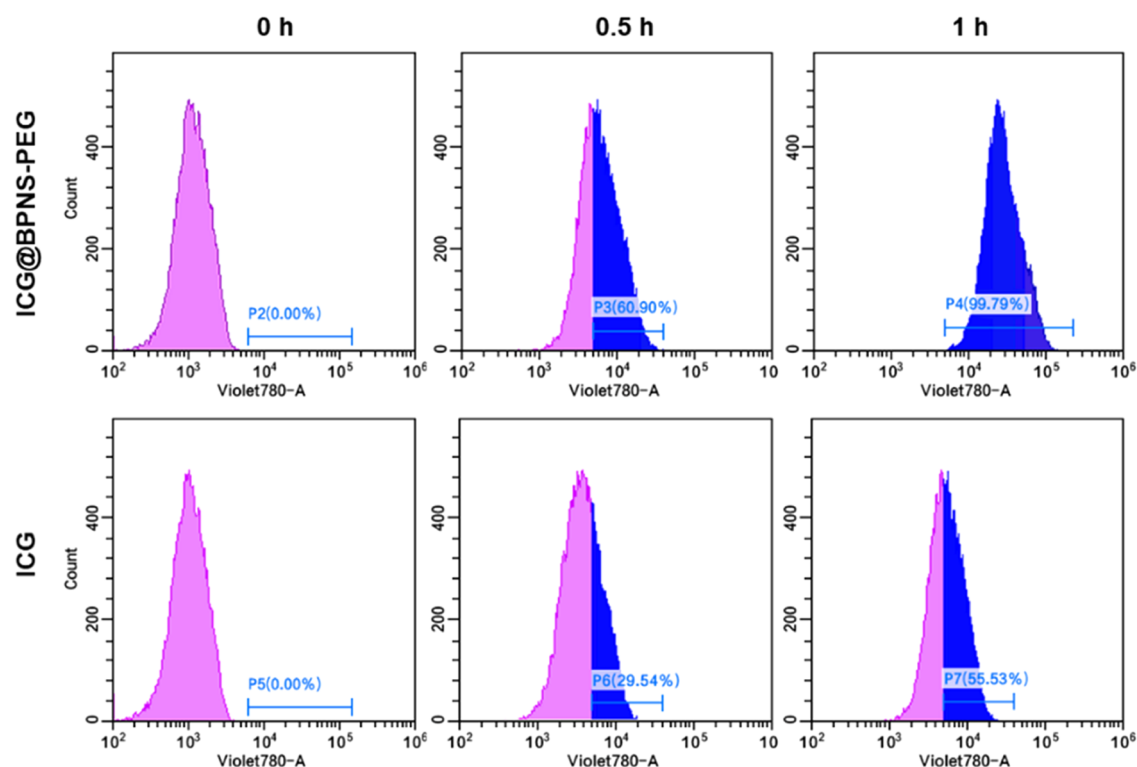
Figure 4. Fluorescence intensity in cells treated with ICG@BPNS-PEG and ICG. The blue section represents the fluorescence intensity of ICG.

as a guard to protect BPNS from oxidation degradation. As shown in Figure 2B,C, the diameters of bare BPNS reduced as the exposure time increased; after 1 week of oxidation, the hydrodynamic radius reduced to nearly half of pristine materials. Fortunately, the hydrodynamic radius of the PEG-coating BPNS was merely reduced by 25 nm, owing to the protection of PEG coating. Analogously, the TEM image of bare BPNS after 7 days in Figure S3A indicates that bare BPNS was oxidized and many bright dots appeared owing to oxidation, leading to thinner layers. Moreover, the ratio of A_{1g} to A_{2g} in Figure S3B decreased from 0.807 to 0.579, indicating that severe oxidation of bare black phosphorus nanosheets occurred without the PEG layered protection.[30,31] The high-resolution P 2p spectra of bare BPNS also confirm that the oxidation of bare black phosphorus nanosheets occurred without the PEG layered protection.

Inspired by the satisfactory results, the surface potentials of relevant materials are also detected as shown in Figure 2D. The potential of BP-PEG increased to −24.5 mV due to PEG coating. In comparison, the surface potential of ICG@BPNS-PEG increased to −16.2 mV after inducing ICG (Figure 2D). This result may be attributed to the $\pi-\pi$ interactions between ICG and BPNS, which could effectively limit the electronic activity, weakening the surface potential. The hydrodynamic radius of ICG@BPNS-PEG was maintained for enhanced water solubility and dispersion stability. In addition, the UV−vis spectrum results also proved that ICG is successfully anchored and the special absorption peak showed a slight blue-shift compared with that of pure ICG as shown in Figure 2E, which is attributed to the interaction between ICG and BPNS. So far, ICG, as a kind of common diagnostic agent, has been applied for angiography in the clinic. Although many studies have reported that ICG could be used for deeper tumor location due to the longer emission wavelength (reaching 820 nm), imaging signal intensity and duration are closely related to the dose of

diagnostic agents. Inspired by the electron-rich surface of BPNS, the loading capacity of BPNS is meticulously studied through designing various feeding ratios (i.e., ICG/BP ratios). As shown in Figure 2F, the loading capacity of BPNS effectively increases as the ICG/BP ratio increases, reaching up to 220%, mainly benefiting from the electron-rich surface and high specific surface area of BPNS, and the best loading efficiency reached 80% (Figure 2D). However, the loading efficiency began to reduce when the loading ratio reached 25:16. This result might be attributed to the limited surface area of BPNS, leading to the denouement that the ICG could not be stably loaded. Moreover, X-ray photoelectron spectroscopy (XPS) was also employed to investigate the surface element variation of ICG@BPNS-PEG. As shown in Figure S2A, the atomic percentages of nitrogen, phosphorus, oxygen, and carbon were ~1.4, 33.8, 34.0, and 30.8%, respectively, which indicate the coexistence of ICG, BPNS, and PEG. In the high-resolution P 2p spectra in Figure S2B, the characteristic peak (i.e., P^0 2p) represents the existence of a BP frame. Moreover, the characteristic absorption peaks attributed to the C−N bond can be found in the high-resolution C 1s (Figure S2C) spectra, which is attributed to the existence of the C−N bond in the molecular structure of ICG. The results indicate the successful loading of ICG on the surface of BP nanosheets as well as the existence of a PEG coating. In addition, as shown in Figure S2D, the high-resolution O 1s spectra showed typical peaks C−O, O−P−O, and O−P═O, indicating the existence of PEG and PO_x. The occurrence of the weak peak assigned to the PO_x bond implies that BP is only slightly oxidized. However, slight oxidation has no obvious influence on physicochemical properties.

Then, the photothermal conversion performances of ICG@BPNS-PEG are evaluated. As shown in Figure 3A, the increasing temperature induced by the photothermal effect of ICG@BPNS-PEG showed obvious concentration-dependent proper-
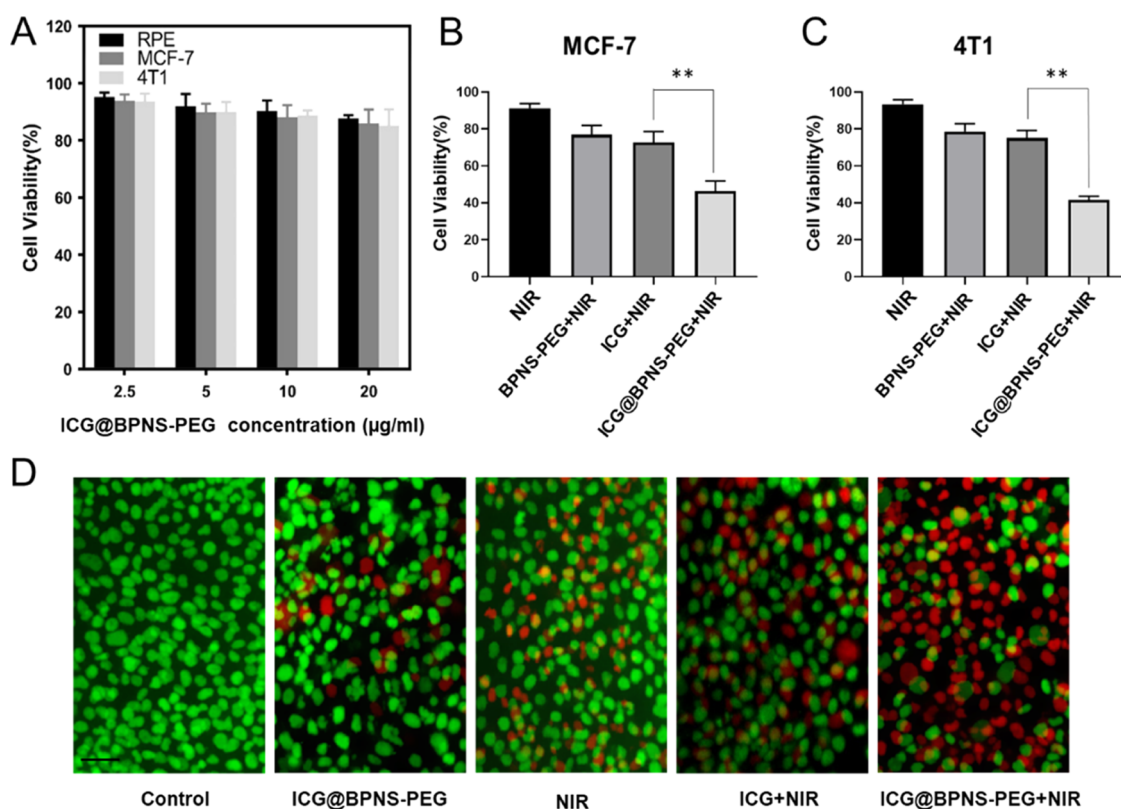
Figure 5. Cell viability of incubation of cells with PBS, BPNS-PEG, ICG, and ICG@BPNS-PEG. (A) Cell viability of RPE, MCF-7, and 4T1 cells treated with various concentrations of ICG@BPNS-PEG. (B) Cell viability of MCF-7 cells treated with BPNS-PEG, ICG, and ICG@BPNS-PEG, with an 808 nm NIR laser for 5 min (**P < 0.001). (C) Cell viability of 4T1 cells treated with BPNS-PEG, ICG, and ICG@BPNS-PEG, with 808 nm NIR laser for 5 min (**P < 0.001). (D) Live and dead staining of 4T1 cells treated with PBS, ICG@BPNS-PEG, NIR, ICG+NIR, and ICG@BPNS-PEG +NIR. Green and red colors represent live and dead cells, respectively. Scale bar: 50 μm.

ties. When the concentration of BPNS of 100 μg/mL was treated with 1.65 W/cm^2 for 5 min, the temperature of ICG@BPNS-PEG increased by 18.21 °C. The increasing temperature could lead to acceptable cytotoxicity because most breast cancer cells cannot bear the hyperthermal environment between 43 and 47 °C according to some reported literature.[32,33] Considering the other composites of the constructed system, PBS, ICG, and BPNS-PEG were compared with ICG@BPNS-PEG. Satisfactorily, the temperature of PBS, BPNS, and ICG only increased by 0.61, 7.59, and 12.99 °C, respectively, when treated with the same methods as shown in Figure 3B. The results showed that ICG@BPNS-PEG has a better photothermal conversion capacity than ICG and BPNS. Moreover, for visual representation, the photothermal images of PBS, BPNS, ICG, and ICG@ BPNS-PEG after 5 min of NIR irradiation are also shown in Figure 3D. Moreover, a number of studies have demonstrated ICG plays an essential role as a potential photothermal therapeutic agent.[34] However, once photothermal therapeutic agents experience photobleaching, the photothermal conversion capacity would become unsatisfactory. Therefore, the photostability was evaluated as shown in Figure 3C. After continuous laser irradiation for four on−off cycles, the temperature of ICG@BPNS-PEG showed no significant change while free ICG gradually decreased in Figure 3C. This result indicates that ICG@BPNS-PEG has excellent photostability owing to the better protection of the PEG coating. The above results indicate that once the nanocomposites are ingested, the ICG@BPNS-PEG nanocomposites, as an ideal photothermal therapeutic

agent, could cause acute breast cancer cell apoptosis after treatment with NIR.

Based on the satisfactory photothermal conversion capacity of ICG@BPNS-PEG, quantitative cellular uptake behavior of ICG and ICG@BPNS-PEG was evaluated through flow cytometry. As shown in Figure 4, the ICG accumulation has an outstanding time-dependent behavior whether it is free ICG or CG@BPNS-PEG. After incubation for half an hour, ICG in the cell was observed whether it is treated with the ICG or ICG@BPNS-PEG, indicating the successful internalization of ICG. However, the fluorescence intensity of ICG in 4T1 cells treated with ICG@BPNS-PEG was twice that of free ICG after incubation for 0.5 h. Surprisingly, all cells ingested ICG@BPNS-PEG after incubation for 1 h, while only 50% of the total cells were taken in after being treated with ICG for 1 h, indicating that nanoscale BPNS could improve the binding to the tumor cells and enhance the cellular uptake of ICG owing to its higher loading capability and the EPR effect.[35−37] Also, the above results demonstrate the excellent passive tumor-targeting ability of ICG@BPNS-PEG.

Through cellular uptake, ICG@BPNS-PEG could play its therapeutic role. Therefore, to evaluate the photothermal therapy-inducing cytotoxicity, ICG@BPNS-PEG, RPE, MCF-7, and 4T1 cells were incubated with the medium containing ICG@BPNS-PEG of different concentrations for 24 h. As shown in Figure 5A, the results show that ICG@BPNS-PEG had no significant cytotoxicity in all groups, indicating that ICG@ BPNS-PEG has lower biotoxicity. The results showed that ICG@BPNS-PEG induced acute cell death than ICG and BPNS treated with 808 nm irradiation whether it is MCF-7 or 4T1 cells
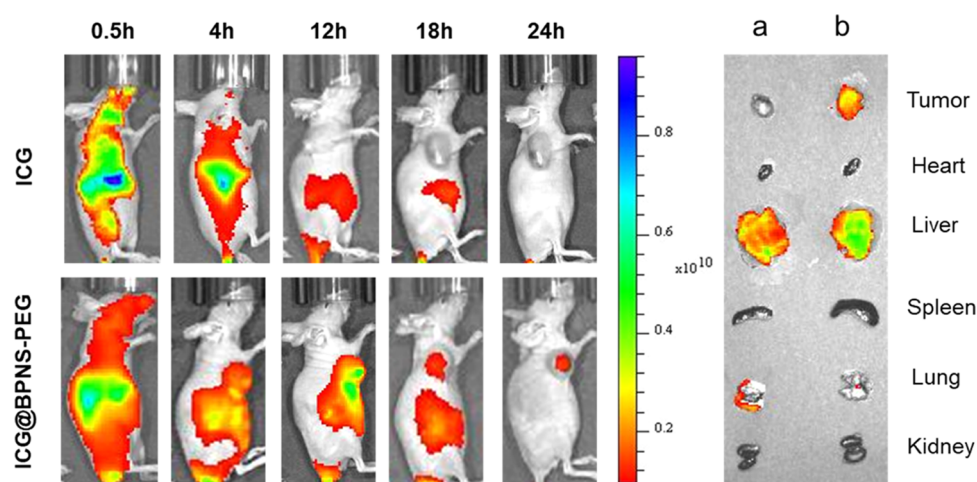
Figure 6. Fluorescence signal in the 4T1-bearing mouse model after intravenous injection of ICG and ICG@BPNS-PEG. (a, b) Injection of ICG and ICG@BPNS-PEG.
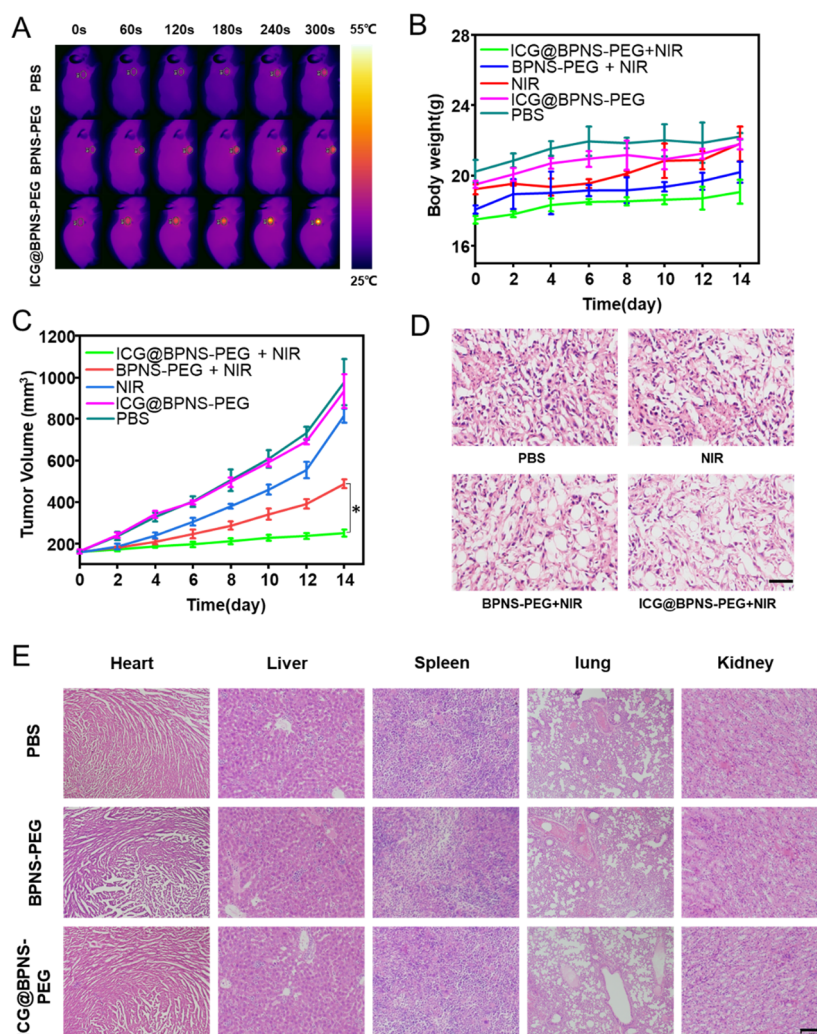
Figure 7. In vivo effect of PTT of ICG and ICG@BPNS-PEG in the 4T1-bearing BABL/C nude mouse model. (A) Thermal imaging of mice 12 h after injection with PBS, BPNS-PEG, and ICG@BPNS-PEG with NIR light for 300 s. (B) Body weight change in mice treated with PBS, ICG@BPNS-PEG, NIR, BPNS-PEG+NIR, and ICG@BPNS-PEG+NIR. (C) The corresponding tumor volume growth curves of mice treated with PBS, ICG@BPNS-PEG, NIR, BPNS-PEG+NIR, and ICG@BPNS-PEG+NIR ($*P < 0.05$). (D) H&E staining of tumor sections after PTT. Scale bar: 20 μm. (E) Representative H&E staining images of major organs, including the heart, liver, spleen, lung, and kidney. Scale bar: 100 μm.

(Figure 5B,C). The quantitative results showed that over ~50% of MCF-7 cells were killed after an 808 nm laser irradiation for 5

min in Figure 5B. In contrast, only 25% of MCF-7 cells were dead treated with free ICG or BPNS-PEG after an 808 nm laser

irradiation. The cytotoxicity of 4T1 cells remained consistent with that of MCF-7 cells. In addition, live and dead staining results also showed that ICG@BPNS-PEG has a superior photothermal effect in Figure 5D, which is consistent with the results through the MTT assay. The above results of cytotoxicity all indicate that ICG@BPNS-PEG nanocomposites are potential for the photothermal therapy of the tumor-bearing mouse model.

Inspired by the exciting results of in vitro cytotoxicity, the passive tumor-targeting ability of ICG@BPNS-PEG nanocomposites through the 4T1 tumor-bearing mouse model was further studied and demonstrated. As shown in Figure 6, the fluorescence signal treated with ICG@BPNS-PEG appeared in the tumor location at 0.5 h postinjection through blood circulation, and then the fluorescence signal gradually enhanced and reached a peak at 12 h postinjection. However, at 24 h postinjection, the tumor area still showed an outstanding fluorescence signal. This result indicates that ICG@BPNS-PEG could efficiently accumulate in the tumor location via the EPR effect after long blood circulation. Meanwhile, the tumor and major organs were collected 12 h after injection. The tumor tissue exhibits moderate fluorescence signal, which demonstrates ICG@BPNS-PEG nanocomposites have the advantages of good tumor accumulation and effective catabolism. However, the stronger fluorescence in the liver was attributed to the potential metabolism process. In contrast, the fluorescence signal postinjection of free ICG just lasted 18 h and then disappeared. In addition, no obvious tumor accumulation appeared, and most of the fluorescence signal was concentrated in the liver rather than in the tumor location. Also, the results indicate that the small-molecule ICG is not an ideal agent for intraoperative positioning imaging and not suitable to ensure optical irradiation treatment time. Also, the ICG@BPNS-PEG nanocomposite is an alternative for tumor theranostics.

Based on the above satisfactory in vitro photothermal effect and in vivo fluorescence imaging, the photothermal therapeutic effect was evaluated through the 4T1-bearing BALB/C nude mouse model. The thermal images are performed at 12 h postinjection of ICG@BPNS-PEG. The temperature of tumor locations increases gradually with the increase of illumination time and reaches 50 °C, which is slightly higher than that of BPNS-PEG+NIR in Figure 7A. Also, this temperature is enough to induce tumor regression. In comparison, the temperature just increased to 40 °C and cannot lead to acute tumor inhibition after illumination. The changes in tumor volume of all mice during 14 days of NIR light are shown in Figure 7B. the tumor volume of mice in the ICG@BPNS-PEG+NIR group was 263.77 mm³, which was significantly smaller than that in the PBS and BPNS-PEG +NIR groups. These results demonstrate that ICG@BPNS-PEG has a superior photothermal therapeutic effect. Meanwhile, the potential toxicity of ICG@BPNS-PEG was studied. During the treatment, there was no decrease in the body weight in Figure 7C, indicating little side effects and good biocompatibility of the constructed nanocomposites. The H&E staining results of the tumor tissue were also consistent with the above results as shown in Figure 7D.

In addition, we also confirmed that ICG@BPNS-PEG has no obvious in vivo biotoxicity. As shown in Figure 7D, the result of H&E staining of the heart, liver, spleen, lung, and kidney in the ICG@BPNS-PEG+NIR group showed no obvious damage when compared with the PBS and BPNS-PEG groups. These results indicate that ICG@BPNS-PEG has the advantage of good biocompatibility.

CONCLUSIONS

In summary, the constructed ICG@BPNS-PEG nanodrug delivery system can enhance the tumor accumulation and long-term retention of ICG in the tumor location. Simultaneously, the PTT of ICG@BPNS-PEG can also effectively inhibit tumor growth. Therefore, the ICG@BPNS-PEG nanocomposite has broad application prospects in the field of breast cancer theranostics. Moreover, the ICG@BPNS-PEG fluorescence imaging-guided surgery can help determine the surgical margin of breast cancer, especially the identification and removal of sentinel lymph nodes, which makes surgical resection more accurate and minimizes tumor residue. Integrating ICG into biocompatible black phosphorus nanosheets provides a safe and reliable strategy for breast cancer theranostics. Furthermore, future clinical studies are promising for loading various FDA-approved chemotherapy drugs and accelerating their clinical transformation.

MATERIALS AND METHODS

First, BP was synthesized from red phosphorous (RP) using a previously reported method, with modifications.[38] The prepared BP suspension was centrifuged to obtain suitable nanolayers of BPNSs. Then, BPNSs and ICG with various mass ratios were mixed to evaluate the ICG loading capacity and the ICG loading efficiency. To improve the stability of ICG@BPNS, we modified it with PEG-NH₂.

ICG loading capacity and ICG loading efficiency were calculated by eqs 1 and 2, respectively

$$\text{ICG loading capacity} = \frac{\text{the amount of loaded ICG}}{\text{the amount of BPNS}} \quad (1)$$

$$\text{ICG loading efficiency} = \frac{\text{the amount of loaded ICG}}{\text{he primary amount of ICG}} \quad (2)$$

Second, we evaluated the cytotoxicity and cell uptake rate in vitro by co-culturing the ICG and ICG@BPNS with RPE, MCF-7, and 4T1 cells. To compare the PTT effects of ICG and ICG@BPNS-PEG, we used the MTT kit and FDA/PI co-staining to evaluate the cell viability.

Finally, ICG and ICG@BPNS-PEG were injected into mice via tail vein, and we collected the distribution of fluorescence in vivo at different times to evaluate the tumor targeting of ICG@BPNS-PEG. Meanwhile, the tumor sites were treated with an 808 nm NIR light at the time of maximum fluorescence enrichment. The body weight and tumor volume of mice were recorded after 14 days of illumination. The volume (V) of the tumor was calculated as follows: $V = D \times d^2/2$, where D and d represent the longest and shortest diameters of the tumor, respectively. After 14 days, hearts, livers, spleens, kidneys, lungs, and tumors were collected to be stained with HE to observe changes in each group.

ASSOCIATED CONTENT

ⓈI Supporting Information

The Supporting Information is available free of charge at https://pubs.acs.org/doi/10.1021/acsomega.1c04909.

> Extensive descriptions of experimental sections including preparation of few-layered BP: ICG loading behavior of BP; cytotoxicity assay, cellular uptake assays and PTT of nanocomposites; in vivo fluorescence imaging and PTT; and the additional graphs of experiments: Figure S1. TEM image of bare BP nanosheets; Raman spectroscopy; XRD

spectroscopy of bulk black phosphorus (BP) and BPNS-PEG; Figure S2. XPS survey spectra of ICG@BPNS-PEG NCs; high-resolution P 2p spectra; high-resolution C 1s XPS spectra; high-resolution O 1s XPS spectra of ICG@BPNS-PEG NCs. Figure S3. TEM image of bare BP nanosheets after 7 days; Raman spectroscopy of various materials after 7 days; high-resolution P 2p spectra of bare BPNS after 7 days (PDF)

■ AUTHOR INFORMATION

Corresponding Authors

Yuan Hu − *State Key Laboratory of Fire Science, University of Science and Technology of China, Hefei 230026 Anhui, P. R. China;* orcid.org/0000-0003-0753-5430; Email: yuanhu@ustc.edu.cn

Xiaopeng Ma − *Department of Thyroid and Breast Surgery, The First Affiliated Hospital of University of Science and Technology of China, Hefei 230036 Anhui, P. R. China;* orcid.org/0000-0002-3517-5439; Email: XiaopengMa@fsyy.ustc.edu.cn

Zhenye Yang − *Hefei National Laboratory for Physical Sciences at Microscale, The CAS Key Laboratory of Innate Immunity and Chronic Disease, School of Basic Medical Sciences, Division of Life Sciences and Medicine, University of Science and Technology of China, Hefei 230026 Anhui, P. R. China;* Email: zhenye@ustc.edu.cn

Guodong Shen − *Department of Geriatrics, The First Affiliated Hospital of University of Science and Technology of China, Hefei 230036 Anhui, P. R. China;* Email: gdshen@ustc.edu.cn

Authors

Wanwan Pan − *Department of Thyroid and Breast Surgery, The First Affiliated Hospital of University of Science and Technology of China, Hefei 230036 Anhui, P. R. China*

Weijian Chen − *State Key Laboratory of Fire Science, University of Science and Technology of China, Hefei 230026 Anhui, P. R. China*

Yuanzeng Min − *CAS Key Laboratory of Soft Matter Chemistry, Department of Chemistry, Department of Bio-X Interdisciplinary Science at Hefei National Laboratory (HFNL) for Physical Science at the Microscale, University of Science and Technology of China, Hefei 230026 Anhui, P. R. China*

Jing Wang − *Department of Thyroid and Breast Surgery, The First Affiliated Hospital of University of Science and Technology of China, Hefei 230036 Anhui, P. R. China*

Tian Xu − *Hefei National Laboratory for Physical Sciences at Microscale, The CAS Key Laboratory of Innate Immunity and Chronic Disease, School of Basic Medical Sciences, Division of Life Sciences and Medicine, University of Science and Technology of China, Hefei 230026 Anhui, P. R. China*

Fazhi Yu − *Hefei National Laboratory for Physical Sciences at Microscale, The CAS Key Laboratory of Innate Immunity and Chronic Disease, School of Basic Medical Sciences, Division of Life Sciences and Medicine, University of Science and Technology of China, Hefei 230026 Anhui, P. R. China*

Complete contact information is available at:
https://pubs.acs.org/10.1021/acsomega.1c04909

Author Contributions

[#]W.P. and W.C. contributed equally to this study. All authors have given approval to the final version of the manuscript.

Notes

The authors declare no competing financial interest.

■ REFERENCES

(1) DeSantis, C. E.; Ma, J.; Gaudet, M. M.; Newman, L. A.; Miller, K. D.; Goding; Sauer, A.; Jemal, A.; Siegel, R. L.; et al. Breast cancer statistics, 2019. *CA: Cancer J. Clin.* **2019**, *69*, 438−451.

(2) Sohn, G.; Son, B. H.; Lee, S. J.; Kang, E. Y.; Jung, S. H.; Cho, S. H.; Baek, S.; Lee, Y. R.; Kim, H. J.; Ko, B. S.; Yu; Lee, J. W.; Ahn, S. H. Treatment and survival of patients with occult breast cancer with axillary lymph node metastasis: a nationwide retrospective study. *J. Surg. Oncol.* **2014**, *110*, 270−274.

(3) Sakai, T.; Ueno, T. Local management after neoadjuvant treatment for breast cancer. *Chin. Clin. Oncol.* **2020**, *9*, No. 34.

(4) Molina, C. A.; Pennington, Z.; Ahmed, A. K.; Westbroek, E.; Goodwin, M. L.; Tamargo, R.; Sciubba, D. M. Use of Intraoperative Indocyanine Green Angiography for Feeder Vessel Ligation and En Bloc Resection of Intramedullary Hemangioblastoma. *Oper. Neurosurg.* **2019**, *17*, 573−579.

(5) Liu, B.; Li, C.; Chen, G.; Liu, B.; Deng, X.; Wei, Y.; Xia, J.; Xing, B.; Ma, P.; Lin, J. Synthesis and Optimization of MoS2@Fe3O4-ICG/Pt(IV) Nanoflowers for MR/IR/PA Bioimaging and Combined PTT/PDT/Chemotherapy Triggered by 808 nm Laser. *Adv. Sci.* **2017**, *4*, No. 1600540.

(6) Yang, J.; Tao, H. S.; Cai, W.; Zhu, W.; Zhao, D.; Hu, H. Y.; Liu, J.; Fang, C. H. Accuracy of actual resected liver volume in anatomical liver resections guided by 3-dimensional parenchymal staining using fusion indocyanine green fluorescence imaging. *J. Surg. Oncol.* **2018**, *118*, 1081−1087.

(7) Gupta, I.; Cahoon, J.; Zhang, X.; Jones, A. D.; Ahmed, F.; Uehara, H.; Messenger, W.; Ambati, B. K. In vivo ZW800-microbead imaging of retinal and choroidal vascular leakage in mice. *Exp. Eye Res.* **2015**, *134*, 155−158.

(8) Campu, A.; Focsan, M.; Lerouge, F.; Borlan, R.; Tie, L.; Rugina, D.; Astilean, S. ICG-loaded gold nano-bipyramids with NIR activatable dual PTT-PDT therapeutic potential in melanoma cells. *Colloids Surf., B* **2020**, *194*, No. 111213.

(9) Shan, W.; Chen, R.; Zhang, Q.; Zhao, J.; Chen, B.; Zhou, X.; Ye, S.; Bi, S.; Nie, L.; Ren, L. Improved Stable Indocyanine Green (ICG)-Mediated Cancer Optotheranostics with Naturalized Hepatitis B Core Particles. *Adv. Mater.* **2018**, *30*, No. 1707567.

(10) Maziukiewicz, D.; Grześkowiak, B. F.; Coy, E.; Jurga, S.; Mrówczyński, R. NDs@PDA@ICG Conjugates for Photothermal Therapy of Glioblastoma Multiforme. *Biomimetics* **2019**, *4*, No. 3.

(11) Chimene, D.; Alge, D. L.; Gaharwar, A. K. Two-Dimensional Nanomaterials for Biomedical Applications: Emerging Trends and Future Prospects. *Adv. Mater.* **2015**, *27*, 7261−7284.

(12) Huang, X.; Tan, C.; Yin, Z.; Zhang, H. 25th anniversary article: hybrid nanostructures based on two-dimensional nanomaterials. *Adv. Mater.* **2014**, *26*, 2185−2204.

(13) Kurapati, R.; Kostarelos, K.; Prato, M.; Bianco, A. Biomedical Uses for 2D Materials Beyond Graphene: Current Advances and Challenges Ahead. *Adv. Mater.* **2016**, *28*, 6052−6074.

(14) Yang, G.; Zhu, C.; Du, D.; Zhu, J.; Lin, Y. Graphene-like two-dimensional layered nanomaterials: applications in biosensors and nanomedicine. *Nanoscale* **2015**, *7*, 14217−14231.

(15) Yang, X.; Wu, R.; Xu, N.; Li, X.; Dong, N.; Ling, G.; Liu, Y.; Zhang, P. Application and prospect of antimonene: A new two-

dimensional nanomaterial in cancer theranostics. *J. Inorg. Biochem.* **2020**, *212*, No. 111232.

(16) Deng, X.; Liang, H.; Yang, W.; Shao, Z. Polarization and function of tumor-associated macrophages mediate graphene oxide-induced photothermal cancer therapy. *J. Photochem. Photobiol., B* **2020**, *208*, No. 111913.

(17) Peng, F.; Zhao, F.; Shan, L.; Li, R.; Jiang, S.; Zhang, P. Black phosphorus nanosheets-based platform for targeted chemo-photothermal synergistic cancer therapy. *Colloids Surf., B* **2021**, *198*, No. 111467.

(18) Hussein, E. A.; Zagho, M. M.; Nasrallah, G. K.; Elzatahry, A. A. Recent advances in functional nanostructures as cancer photothermal therapy. *Int. J. Nanomed.* **2018**, *13*, 2897−2906.

(19) Zhu, X.; Feng, W.; Chang, J.; Tan, Y. W.; Li, J.; Chen, M.; Sun, Y.; Li, F. Temperature-feedback upconversion nanocomposite for accurate photothermal therapy at facile temperature. *Nat. Commun.* **2016**, *7*, No. 10437.

(20) Shao, J.; Xie, H.; Huang, H.; Li, Z.; Sun, Z.; Xu, Y.; Xiao, Q.; Yu, X. F.; Zhao, Y.; Zhang, H.; Wang, H.; Chu, P. K. Biodegradable black phosphorus-based nanospheres for in vivo photothermal cancer therapy. *Nat. Commun.* **2016**, *7*, No. 12967.

(21) Cheng, W.; Liang, C.; Xu, L.; Liu, G.; Gao, N.; Tao, W.; Luo, L.; Zuo, Y.; Wang, X.; Zhang, X.; Zeng, X.; Mei, L. TPGS-Functionalized Polydopamine-Modified Mesoporous Silica as Drug Nanocarriers for Enhanced Lung Cancer Chemotherapy against Multidrug Resistance. *Small* **2017**, *13*, No. 1700623.

(22) Shao, J.; Xie, H.; Huang, H.; Li, Z.; Sun, Z.; Xu, Y.; Xiao, Q.; Yu, X. F.; Zhao, Y.; Zhang, H.; Wang, H.; Chu, P. K. Biodegradable black phosphorus-based nanospheres for in vivo photothermal cancer therapy. *Nat. Commun.* **2016**, *7*, No. 12967.

(23) Yin, W.; Yan, L.; Yu, J.; Tian, G.; Zhou, L.; Zheng, X.; Zhang, X.; Yong, Y.; Li, J.; Gu, Z.; Zhao, Y. High-throughput synthesis of single-layer MoS2 nanosheets as a near-infrared photothermal-triggered drug delivery for effective cancer therapy. *ACS Nano* **2014**, *8*, 6922−6933.

(24) Li, B.; Ye, K.; Zhang, Y.; Qin, J.; Zou, R.; Xu, K.; Huang, X.; Xiao, Z.; Zhang, W.; Lu, X.; Hu, J. Photothermal theragnosis synergistic therapy based on bimetal sulphide nanocrystals rather than nanocomposites. *Adv. Mater.* **2015**, *27*, 1339−1345.

(25) Shao, J.; Ruan, C.; Xie, H.; Li, Z.; Wang, H.; Chu, P. K.; Yu, X. F. Black-Phosphorus-Incorporated Hydrogel as a Sprayable and Biodegradable Photothermal Platform for Postsurgical Treatment of Cancer. *Adv. Sci.* **2018**, *5*, No. 1700848.

(26) Yang, X.; Wang, D.; Shi, Y.; Zou, J.; Zhao, Q.; Zhang, Q.; Huang, W.; Shao, J.; Xie, X.; Dong, X. Black Phosphorus Nanosheets Immobilizing Ce6 for Imaging-Guided Photothermal/Photodynamic Cancer Therapy. *ACS Appl. Mater. Interfaces* **2018**, *10*, 12431−12440.

(27) Fan, J.; Liu, B.; Long, Y.; Wang, Z.; Tong, C.; Wang, W.; You, P.; Liu, X. Sequentially-targeted biomimetic nano drug system for triple-negative breast cancer ablation and lung metastasis inhibition. *Acta Biomater.* **2020**, *113*, 554−569.

(28) Doganov, R. A.; O'Farrell, E. C.; Koenig, S. P.; Yeo, Y.; Ziletti, A.; Carvalho, A.; Campbell, D. K.; Coker, D. F.; Watanabe, K.; Taniguchi, T.; Castro Neto, A. H.; Özyilmaz, B. Transport properties of pristine few-layer black phosphorus by van der Waals passivation in an inert atmosphere. *Nat. Commun.* **2015**, *6*, No. 6647.

(29) Liu, H.; Neal, A. T.; Zhu, Z.; Luo, Z.; Xu, X.; Tománek, D.; Ye, P. D. Phosphorene: an unexplored 2D semiconductor with a high hole mobility. *ACS Nano* **2014**, *8*, 4033−4041.

(30) Zhu, X.; Zhang, T.; Sun, Z.; Chen, H.; Guan, J.; Chen, X.; Ji, H.; Du, P.; Yang, S. Black Phosphorus Revisited: A Missing Metal-Free Elemental Photocatalyst for Visible Light Hydrogen Evolution. *Adv. Mater.* **2017**, *29*, No. 1605776.

(31) Favron, A.; Gaufres, E.; Fossard, F.; Phaneuf-L'Heureux, A. L.; Tang, N. Y.; Levesque, P. L.; Loiseau, A.; Leonelli, R.; Francoeur, S.; Martel, R. Photooxidation and quantum confinement effects in exfoliated black phosphorus. *Nat. Mater.* **2015**, *14*, 826−832.

(32) Doughty, A. C. V.; Hoover, A. R.; Layton, E.; Murray, C. K.; Howard, E. W.; Chen, W. R. Nanomaterial Applications in Photothermal Therapy for Cancer. *Materials* **2019**, *12*, No. 779.

(33) de Melo-Diogo, D.; Pais-Silva, C.; Dias, D. R.; Moreira, A. F.; Correia, I. J. Strategies to Improve Cancer Photothermal Therapy Mediated by Nanomaterials. *Adv. Healthcare Mater.* **2017**, *6*, No. 1700073.

(34) Campu, A.; Focsan, M.; Lerouge, F.; Borlan, R.; Tie, L.; Rugina, D.; Astilean, S. ICG-loaded gold nano-bipyramids with NIR activatable dual PTT-PDT therapeutic potential in melanoma cells. *Colloids Surf., B* **2020**, *194*, No. 111213.

(35) Wu, R. S.; Lin, J.; Xing, Y. M.; Dai, Z. L.; Wang, L. W.; Zhang, X. P. pH-Sensitive Black Phosphorous-Incorporated Hydrogel as Novel Implant for Cancer Treatment. *J. Pharm. Sci.* **2019**, *108*, 2542−2551.

(36) Sun, C.; Wen, L.; Zeng, J.; Wang, Y.; Sun, Q.; Deng, L.; Zhao, C.; Li, Z. One-pot solventless preparation of PEGylated black phosphorus nanoparticles for photoacoustic imaging and photothermal therapy of cancer. *Biomaterials* **2016**, *91*, 81−89.

(37) Gao, N.; Xing, C.; Wang, H.; Feng, L.; Zeng, X.; Mei, L.; Peng, Z. pH-Responsive Dual Drug-Loaded Nanocarriers Based on Poly (2-Ethyl-2-Oxazoline) Modified Black Phosphorus Nanosheets for Cancer Chemo/Photothermal Therapy. *Front. Pharmacol.* **2019**, *10*, No. 270.

(38) Qui, S.; Yi, Z.; Xia, Z.; Tao, Z.; Chen, W.; Richard, K. K. Y.; Wei, H.; Yuan, H. Air-Stable Polyphosphazene-Functionalized Few-Layer Black Phosphorene for Flame Retardancy of Epoxy Resins. *Small* **2019**, *15*, No. 1805175.